

# Revealing stress-induced changes equivalence between polarization-sensitive optical coherence tomography and polarimetric camera measurements

Verónica Mieites<sup>a,b</sup>, José A. Gutiérrez-Gutiérrez<sup>a,b</sup>, Arturo Pardo<sup>a</sup>, José M. López-Higuera<sup>a,b,c</sup>, Olga M. Conde<sup>a,b,c,\*</sup>

<sup>a</sup> Photonics Engineering Group (TEISA Dept.), University of Cantabria, Avda. de los Castros, Santander, 39006, Cantabria, Spain

<sup>b</sup> Valdecilla Research Institute (IDIVAL), Calle Cardenal Herrera Oría, Santander, 39011, Cantabria, Spain

<sup>c</sup> CIBER-BBN, C. de Melchor Fernández Almagro, 3, Madrid, 28029, Madrid, Spain

## ARTICLE INFO

### Keywords:

Polarimetric camera  
Polarization-sensitive  
Optical coherence tomography  
Strain-stress measurements

## ABSTRACT

Polarization-Sensitive Optical Coherence Tomography (PS-OCT) is a widely-used technique for high-resolution material characterization since it allows for real-time structural analysis and imperfections identification. Nevertheless, when the sample is too big or imperfections are not on the micrometric scale, PS-OCT imaging can become too complex to be performed on a regular basis. Alternatively, polarimetric camera (PCam) imaging can obtain polarization measurements of a sample at a macroscopic scale, allowing for a faster and cheaper inspection of the sample. In doing so, the depth-profiling capabilities of PS-OCT would be forfeited, as well as the ability to measure other than the linear polarization qualities of the light beam. This paper compares the data that can be easily extracted from a PCam, with the complete and more complex characterization of the polarization of light that can be obtained with a PS-OCT device. The comparison of both systems is assessed through the evaluation of their performance when measuring different stress states of a sample.

## 1. Introduction

Optical Coherence Tomography (OCT) is a technique based on the interferometric properties of light that is used to capture volumetric images of a sample by scanning it with a laser source with micrometric resolution [1]. Although this technology grew initially in the field of ophthalmology as a tool to study corneal and retinal properties [2–5], many research groups started using it to search for internal and surface structures in material testing. Since OCT uses non-ionizing light and does not make contact with the sample, it was used to evaluate the profilometry of surfaces and coatings [6,7], to evaluate glass and substrates quality [8,9], to analyze weld depth in metallic materials [10,11] and to find flaws and defects in materials in general [12–15].

Polarization-Sensitive OCT (PS-OCT) is a functional extension of the standard OCT technology that includes extra volume optics or fiber-based elements to control the polarization of the laser source [16,17]. By adding polarization-sensitive detector components, one can establish the Stokes parameters of the light that back-scatters from the sample at each spatial point. This modality became a valuable tool in material

science to analyze stress patterns inside polymer and plastic samples [18,19], mainly because of its ability to create internal stress mappings [20]. Any impurity or defect inside a sample would change its polarimetric properties at that location, so the polarization maps of the material would have visually different behaviors at that position, caused by the internal stress that said defect generates on the sample. Not only that but externally applied deformations would also manifest as internal polarimetric differences related to the direction of the applied stress [20].

The main drawback of PS-OCT when it comes to material testing is sample size. Typical field of view values in an OCT system is in the range of the millimeters, which means that to analyze bigger pieces you need to mosaic 3D PS-OCT measurements together [21], which can be a lengthy and tedious process if done manually. The complexity of the data captured with a PS-OCT device has to be taken into consideration too, since developing maps of polarimetric magnitudes usually requires point-by-point calculations that, depending on the sample size, can be very computationally intensive. Both of these issues can be tackled by using a polarimetric camera instead.

\* Corresponding author.

E-mail address: [olga.conde@unican.es](mailto:olga.conde@unican.es) (O.M. Conde).

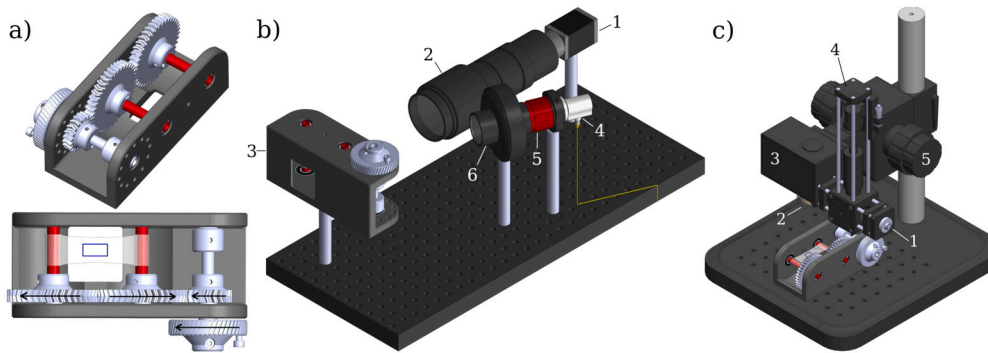


**Fig. 1.** 3D model of the device designed to apply uniform increments of stress on a sample (a). The adhesive tape is secured on the two posts marked in red and, by using the exterior wheel, stress is applied on the sample in opposite directions. The exterior wheel has an insert that allows us to add a pin that fixes both the position of the wheel and the applied stress. The 3D printed device is paired with the PCam equipment (b) or with the PS-OCT device (c). The PCam setup is comprised of the camera (1), a micro-imaging lens (2), the LED and angled mirror light source (4), the beam expander (5), and the polarizer (6). The PS-OCT device has a fiber optics adaptor (1) for the laser source, a collector lens (2) that fixes the penetration depth and resolution, and a height-adjustable, volume optics interferometer (5), comprised by the sample (3) and reference (4) arms.

A conventional polarization or polarimetric camera (PCam) is essentially a regular camera that has an array of polarizers laid on top of the surface of the sensor [22]. These kinds of devices are generally used in the industry as a method to detect defects such as scratches, to find pressure points on materials, and to remove reflections in all kinds of surfaces by just taking a single snapshot, since all of these characteristics cause differences in the polarization state of the reflected light [23]. Aside from industrial uses, recently developed PCam-based experimental setups have been applied to the measurement of shock-wave-induced polarization effects [24], to underwater imaging and enhancement through the degree of linear polarization [25–27], to birefringence measurements in liquids [28] and to color and polarization combined measurements [29,30]. Similar applications to that of the PS-OCT systems have been developed with PCam setups for tasks such as stress measurements [31], by adding optical retarders to capture the complete polarimetric effects on the sample.

Typically, the polarizers array consists on patches of 2x2 linear polarizers at 0°, 45°, 90°, and 135°, so that three of the four Stokes parameters that are related to the linear conditions of light can be calculated [32].

As with any conventional camera, an added benefit of using a PCam is the versatility to pair it with multiple lenses, and therefore adapt to wide-field [33] or microscopic samples [34]. Not only that, but since the limiting factor is the amount of light that enters the sensor, one could take videos that capture the evolution of the polarimetric properties of a sample with time, as fast as the frame rate of the camera allows it.

Importantly, when comparing a PCam with a PS-OCT device, the latter will have a much greater lateral resolution when using conventional lenses (i.e., not macro or microscope lenses), as well as the ability to perform depth measurements. When to use one or the other will depend on the nature of the analysis to be performed. Unfortunately, to the authors' knowledge, there are no publications that systematically relate both modalities in terms of polarimetric equivalence.

In this article, we seek to find an analytical relationship between PS-OCT and PCam-based systems such that their measurements can be related. In other words, the main objective of this manuscript is to provide empirical expressions that allow us to predict the polarization magnitudes of one imaging modality given data coming from the other. As a reference material with high repeatability, we used adhesive tape that we could stretch at different levels of strain in a controlled manner.

## 2. Materials and methods

### 2.1. Equipment

A custom 3D-printed device (Fig. 1, a) was used to apply discrete increments of longitudinal stress in regular intervals to a single tape piece of 7 cm that is secured between two rotating posts.

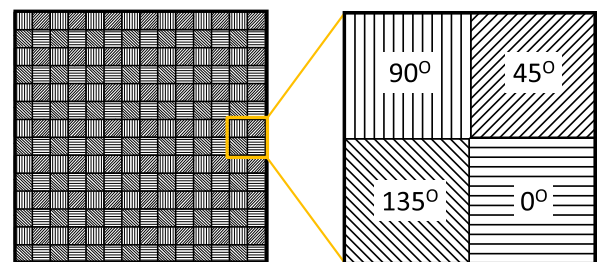


**Fig. 2.** 2x2 polarizer array used over Sony's PolarSens Cameras. On each of the four pixels, the sensor uses linear polarizers set, clockwise, at 90°, 45°, 135° and 0° with respect to the horizontal.

In order to obtain the PS-OCT data we used the commercially available TEL221PS system from Thorlabs (Fig. 1, c). This device has a 1300 nm superluminescent diode source, with a depth resolution of 5.5  $\mu\text{m}$  and a lateral resolution of 13  $\mu\text{m}$  with the selected lens (OCT-LK3) both measured in air. This system comes with a volume optics polarization-sensitive module (OCTP-1300PS) that allows for user customization, such as the modification of the optical beam path or interchangeable lenses. The polarization state of the light back-scattered from the sample gets split into its horizontal and vertical components, which allows for full Stokes components determination ( $S_0$ ,  $S_1$ ,  $S_2$ , and  $S_3$ , or  $I$ ,  $Q$ ,  $U$  and  $V$ ). The polarization-sensitive module has two wave-plates oriented such as the light that strikes the sample is circularly polarized ( $Q/I = 0$ ,  $U/I = 0$ ,  $V/I = 1$ ).

The polarimetric camera (PCam) used was a Sony PolarSens (XCG-CP510), paired with volume optics to create a reflectance setup (Fig. 1, b). The CMOS sensor of the camera has a linear polarizer engraved on each pixel, sitting under the on-chip lens, so that each pixel captures a different linear polarization. The polarizer array consists of a 2x2 macro-pixel repeated across the CMOS sensor, with linear polarization aligned at 0°, 90°, 45° and 135° (Fig. 2). With these polarizers, the three Stokes parameters related to the linear behavior of light can be obtained ( $S_0$ ,  $S_1$ ,  $S_2$ ).

The light source used in the PCam setup is a red laser diode (LP660-SF50, Thorlabs), which has a wavelength of 660 nm, a bandwidth of 20 nm and a typical optical power of 50 mW. The laser is collimated with a protected silver reflective collimator (RC08FC-P01, Thorlabs) and, after that, expanded to form a spot of 17 mm in diameter with a x2 beam expander (GBE03-B, Thorlabs). We used an optical diffuser, made from 1500 Grit N-BK7 ground glass, right after the beam expander to reduce the coherence properties of the laser and remove the diffraction patterns created by the edges of the mounts. After that, we added

a linear polarizer to set the incident polarization state as horizontally polarized light ( $Q/I = 1$ ,  $U/I = 0$ ,  $V/I = 0$ ).

The setup is paired with an Optem FUSION micro-imaging lens system, comprised of five different lens modules (QIO-35-08-70, QIO-35-08-13, QIO-35-31-10-000, QIO-35-03-10, QIO-35-00-05). The lens allows for different magnification settings, with a resolution of 12  $\mu\text{m}/\text{px}$  and 3.1  $\mu\text{m}/\text{px}$ , and a field of view of (6.3  $\times$  7.6) mm and (1.6  $\times$  1.9) mm, for the smallest and greatest zoom possible, respectively.

## 2.2. Samples and measurement procedure

To establish the relationship between the PS-OCT and the PCam measurements, we used adhesive tape (Scotch Magic Tape, 3D ID 7100024666, width = 19 mm) under different stress conditions ( $\tau$ ) as a phantom. After setting the sample in the 3D-printed device, a 5x5 mm square was marked at the center of the tape. This square was used as a reference for manual region of interest (ROI) selection in post-processing with both systems. The size and positioning of the 5x5 mm square were selected to simultaneously ensure that the region of tape under analysis was as far away as possible from both strain posts while making sure that, even when stretching the tape fully, the ROI could still fit inside the field of view of the PS-OCT.

We characterized the stress that our 3D printed device can apply in terms of the measured strain  $\epsilon$  it produces on the tape and its Young's modulus,  $E = 10.1$  MPa [35]. For each individual applied stress index  $\tau$ , we measured its length  $l_0$  with respect to its initial length  $L$  and calculated the strain  $\epsilon = (l_0 - L) \cdot L^{-1}$  and the longitudinal stress  $\sigma = E \cdot \epsilon$ . Note that  $\epsilon$  is dimensionless as long as  $L$  and  $l_0$  have the same units (mm or px in our case). To measure  $l_0$ , a metallic permanent marker was used to paint lines on the tape oriented in the direction of the elongation. From our PS-OCT measurements, we calculated the depth-averaged intensity  $\langle I \rangle$  which allowed for easy image segmentation of the highly-scattering permanent marker lines. The amount of strain on the lines,  $\epsilon$ , was determined for each  $\tau$  and averaged across all marked lines as a measurement of  $\epsilon(\tau)$  of the tape.

To obtain the polarimetric properties, the same spot of the sample was measured using the PS-OCT setup and the PCam, for each  $\tau$ , before applying the next strain value. By using the 3D printed device, the tape is stretched from both ends so that the analysis region always stays in the same position.

We chose this kind of tape as a phantom of applied stress mainly because it shows polarization patterns when studied under stress conditions. Furthermore, tape is a malleable plastic that is strong enough to keep its shape when stretched and resists high longitudinal stress, allowing us to make multiple  $\tau$  measurements. Translucent instead of fully transparent tape was chosen for this experiment to facilitate the focusing process with the PS-OCT and the PCam.

## 2.3. Polarimetric analysis

The Stokes parameters ( $I, Q, U, V$  or  $S_1, S_2, S_3, S_4$ ) are used to define the polarization state of partially or totally polarized light. The following information can be found in multiple references [36,37], but it has been introduced below for completion.

For a  $z$ -propagating electric field given by  $\vec{E} = E_x \hat{x} + E_y \hat{y}$  (Fig. 3), the Stokes parameters are defined as (1):

$$\begin{aligned} S_0 = I &= \langle E_h^2 \rangle + \langle E_v^2 \rangle = I_h + I_v \\ S_1 = Q &= \langle E_h^2 \rangle - \langle E_v^2 \rangle = I_h - I_v \\ S_2 = U &= \langle E_{45}^2 \rangle - \langle E_{135}^2 \rangle = I_{45} - I_{135} \\ S_3 = V &= \langle E_l^2 \rangle - \langle E_r^2 \rangle = I_l - I_r \end{aligned} \quad (1)$$

where  $\langle \cdot \rangle$  denotes time average,  $I_i$  intensity of the electrical field component  $i$ ,  $h$  horizontally polarized light ( $x$ -polarized),  $v$  vertically polarized light ( $y$ -polarized), 45 is linearly polarized light at a 45° angle

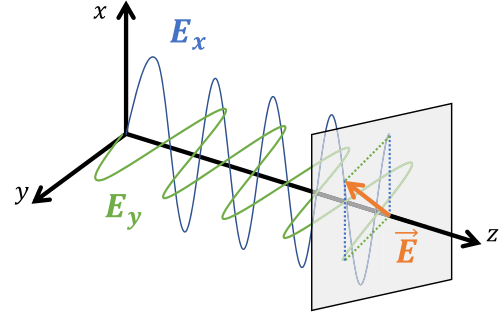


Fig. 3. Coordinate system and electric field definition for the Stokes parameters.

from  $x$ , 135 is linearly polarized light at a 135° angle from  $x$ ,  $l$  is left-handed circularly polarized light and  $r$  is right-handed circularly polarized light.

Usually, one will work with the  $I$ -normalized versions of ( $I, Q, U, V$ ), namely ( $\bar{I}, \bar{Q}, \bar{U}, \bar{V}$ ), which are defined in the following domains:

$$\begin{aligned} \bar{I} &= \frac{I}{I_{max}} \in [0, 1] ; \quad \bar{Q} = \frac{Q}{I} \in [-1, 1] \\ \bar{U} &= \frac{U}{I} \in [-1, 1] ; \quad \bar{V} = \frac{V}{I} \in [-1, 1] \end{aligned} \quad (2)$$

The degree of polarization uniformity ( $DOPU$ ) indicates how much light polarization varies across the spatial dimensions, and can be calculated by doing a spatial average of the Stokes parameters as follows:

$$DOPU = \frac{\sqrt{\langle Q \rangle^2 + \langle U \rangle^2 + \langle V \rangle^2}}{\langle I \rangle} \in [0, 1] \quad (3)$$

where  $\langle \cdot \rangle$  indicates the spatial averaging. When the light is completely polarized and has the same polarization across one neighborhood,  $DOPU = 1$ . On the other hand, completely depolarized light will have  $DOPU = 0$ . In a similar manner, one could define the degree of linear polarization uniformity ( $DOLPU$ ) by studying only the linear properties of light as:

$$DOLPU = \frac{\sqrt{\langle Q \rangle^2 + \langle U \rangle^2}}{\langle I \rangle} \in [0, 1] \quad (4)$$

If the light is completely linearly polarized and is uniform across the sample,  $DOLPU = 1$ . However, any kind of depolarization, lack of uniformity across neighborhoods, or any amount of non-zero circular component will yield  $DOLPU < 1$ .

Both  $DOPU$  and  $DOLPU$  quantify the uniformity of polarization properties across the spatial dimensions. Individually,  $DOPU$  and  $DOLPU$  can serve as indicators of structural anisotropy in a sample, given that defects, changes in thickness, thermal anomalies, or pressure gradients can locally affect the polarization state, thereby influencing both  $DOPU$  and  $DOLPU$ . Besides sample-related effects, they can also serve as indicators of image quality. Detectors with an elevated noise profile will result in noisier polarization states, leading to less defined  $DOPU$  and  $DOLPU$ . The choice between using one or the other will depend on the need for complementing the linear polarization properties ( $Q, U$ ) of the light source, sample, and detector, with their circular counterpart ( $V$ ).

The Stokes parameters can be rewritten to define spherical coordinates in terms of the angles given by the polarization ellipse ( $\Psi$  and  $\chi$ ), which defines the movement of the electromagnetic vector over time in one fixed  $z$ -plane (Fig. 4), as:

$$\begin{aligned} S_0 = I &= a_1^2 + a_2^2 = a^2 + b^2 \\ S_1 = Q &= a_1^2 - a_2^2 = S_0 \cdot \cos(2\chi) \cdot \cos(2\Psi) \\ S_2 = U &= 2a_1 a_2 \cdot \cos(\delta) = S_0 \cdot \cos(2\chi) \cdot \sin(2\Psi) \\ S_3 = V &= 2a_1 a_2 \cdot \sin(\delta) = S_0 \cdot \sin(2\chi) \end{aligned} \quad (5)$$

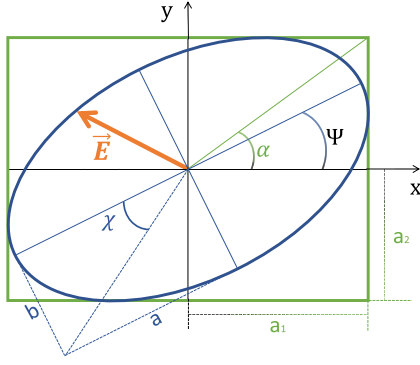


Fig. 4. Coordinate systems and polarization ellipse parameters.

where  $(a, b)$  are the ellipse's major and minor axis,  $\chi$  is the angle that defines the ellipticity,  $(2a_1, 2a_2)$  are the sides of the rectangle in which the ellipse is inscribed,  $\alpha$  is the angle that defines the diagonal of the rectangle and  $\Psi$  is the inclination of the ellipse with respect to  $x$ . The angle  $\delta$  is not depicted in Fig. 4 because it represents the phase delay between components  $E_x$  and  $E_y$  (Fig. 3). If  $\{\delta = m\pi; m \in \mathbb{Z}^+\}$ , the ellipse collapses into a line and light is linearly polarized. In the case that  $\{\delta \in (0, \pi)\}$ , light is left-handed polarized and, if  $\{\delta \in (\pi, 2\pi)\}$ , light is right-handed polarized. To have circularly polarized light, the ellipse and the rectangle must have equal axes,  $a_1 = a_2 = a = b$ , and  $E_x$  and  $E_y$  must be in opposed-phase,  $\{\delta = (2m + 1)\frac{\pi}{2}; m \in \mathbb{Z}^+\}$ .

With equations (1) and (5), we can obtain  $(\Psi, \chi, \delta, \alpha)$  from the Stokes parameters. Our PS-OCT system allows for  $(I, Q, U, V)$  determination but, with the PCam, we can only find  $I, Q$ , and  $U$  because its sensor is covered only with polarizing filters and not phase optics. Because of that, we calculated an expression for every polarimetric magnitude by using only equations (5), along with  $\tan(\chi) = a/b$  and  $\tan(\alpha) = a_1/a_2$ , but without involving  $V$  (full derivations are provided in appendix A). We used equations (6)–(11) to compare the measurements of  $I, Q$ , and  $U$  provided by the PS-OCT and PCam systems.

$$\Psi = \frac{1}{2} \tan^{-1} \left( \frac{U}{Q} \right) \in \left[ -\frac{\pi}{2}, +\frac{\pi}{2} \right] \quad (6)$$

$$\chi = \frac{1}{2} \cos^{-1} \left( \frac{1}{\cos(2\Psi)} \frac{Q}{I} \right) \quad (7)$$

$$= \frac{1}{2} \cos^{-1} \left( \frac{1}{\sin(2\Psi)} \frac{U}{I} \right) \in \left[ 0, \frac{+\pi}{4} \right] \quad (8)$$

$$\delta = \frac{1}{2} \cos^{-1} \left( \frac{n^2 - m^2 - 2n^2 m^2}{m^2 + n^2} \right) \in \left[ 0, \frac{+\pi}{2} \right] \quad (9)$$

$$\{n = \tan(2\Psi); m = \sin(2\chi)\} \quad (10)$$

$$\alpha = \frac{1}{2} \sin^{-1} \left( \frac{\sin(2\chi)}{\sin(\delta)} \right) \quad (11)$$

$$= \frac{1}{2} \tan^{-1} \left( \frac{\tan(2\chi)}{\cos(\delta)} \right) \in \left[ \frac{+\pi}{4}, \frac{+\pi}{2} \right] \quad (12)$$

$$a^2 = \frac{I}{1 + \tan^2(\chi)}; b^2 = \frac{I \cdot \tan^2(\chi)}{1 + \tan^2(\chi)} \quad (10)$$

$$a_1^2 = \frac{I}{1 + \tan^2(\alpha)}; a_2^2 = \frac{I \cdot \tan^2(\alpha)}{1 + \tan^2(\alpha)} \quad (11)$$

### 3. Results

We started our procedure by measuring the Stokes parameters  $(I, Q, U, V)$  of the adhesive tape sample with the PS-OCT device without any stress applied and, right after that, we took a picture with the PCam and calculated  $(I, Q, U)$  with equations (1). Next, we increased the applied stress to repeat the procedure until the tape broke. A pin was used to fix the applied stress to the sample in order to measure it

with both devices. We will refer to the position of the pin as “applied stress index” ( $\tau$ ).

Our PS-OCT system was used to characterize the applied stress  $\tau$  in terms of tape strain  $\epsilon$  and longitudinal stress  $\sigma$ . Both magnitudes are related through Young's modulus as  $E = \sigma/\epsilon = 10.1$  MPa [35]. By measuring  $\epsilon(\tau)$  as described in Section 2.2, linear relationships were identified both between  $\epsilon$  and  $\tau$  (Fig. 5, a) or  $\sigma$  and  $\tau$  (Fig. 5, b).

The first  $\tau$  value has a corresponding  $\epsilon < 0$ , which is not physically possible. This is probably due to the fact that the tape may not be subjected to sufficient tension when applied to the 3D printed device, and subtle creasing is visible until tension is applied uniformly ( $\tau > 1$ ). This means that our custom 3D-printed stretcher is a suitable tool for applying controlled stress increments on tape samples but is likely unsuitable for highly precise, low-intensity strain. To easily identify the different applied stress ( $\tau$ ) conditions, the color code shown in Fig. 5 is used across the figures of this paper, where low-stress values are assigned to darker colors, while higher ones are assigned to lighter colors. The  $\tau$  values will be converted to  $\sigma$  according to the derived linear relationship ( $\sigma = (-0.31 + 0.36\tau)$  MPa, Fig. 5, b).

PS-OCT allows us to obtain the polarimetric magnitudes at different depths inside the sample,  $Z$ , while the PCam setup will integrate the signal coming from all depths. However, since the highest refractive index change happens when the light first enters the sample, and the roughness of the tape is strongest on its surface, the PS-OCT system captures the highest intensity at the air-tape interface (average of  $1.4 \times 10^9$  counts at  $Z = 0$  px). The second highest intensity is achieved when the light exits the tape on the other side (average of  $3.1 \times 10^5$  counts at  $Z = 23$  px  $\approx 80$   $\mu\text{m}$ ), which is still almost 450 times less intense than the light at the first interface. This phenomenon is demonstrated in Fig. 6.

Therefore, two regimes of analysis can be considered: one that focuses on the single-scattering surface effects, and another that studies the polarimetric behavior of light after traversing through the bulk of the sample. To accomplish this, 3D segmentation of the tape samples was conducted by identifying the two most prominent peaks as the air-sample and sample-air interfaces for each A-scan. Subsequently, the analysis was exclusively performed on the first surface indicated by the most intense peak ( $Z = 0$  px) or across the entire tape ( $Z \in [0, 23]$  px), encompassed between the surfaces defined by both peaks. As light penetrates inside the sample, it will tend to lose its polarization uniformity due to an increased probability of change in the propagation direction caused by the scattering. Fig. 7 shows the change in  $DOP_U$  for a piece of tape that was stretched with our 3D-printed device, as measured by our PS-OCT system. In Fig. 7 (a), we considered only the surface layer of the tape ( $Z = 0$  px), while in Fig. 7 (b) we averaged all  $Z$  values for each applied tensile stress ( $Z \in [0, 23]$  px).

Using all  $Z$  values to calculate the polarimetric magnitudes yields less polarization uniformity than using only  $Z = 0$  px, due to both the previously shown decrease in intensity and the increase in scattering inside the sample. To compare the PCam information with the PS-OCT, all of the following results presented in this section for the PS-OCT system are those corresponding to  $Z = 0$  px, i.e., the surface of the tape. This allows us to contrast the volume-integrated signal captured by the PCam with the single-backscattered measurements received from only the surface of the tape with PS-OCT.

Fig. 8 shows the normalized  $\bar{Q}$  and  $\bar{U}$  values for one of the used tape samples. In that figure, the average value of  $\Psi$  (6) is indicated as an arrow on the  $Q - U$  plane, for each measurement. This sample was measured under twelve different  $\tau$  conditions before it broke, which translates into  $714 \times 714$  PS-OCT data points and  $612 \times 512$  PCam data points, for each  $\tau$ . The number of pixels used for the region of interest increased with the applied stress since stretching the tape caused the reference markings on the tape to increase in area as well. As the stress increased, the polarization properties changed slightly between the different measurements. The data distribution is wider but thinner for the

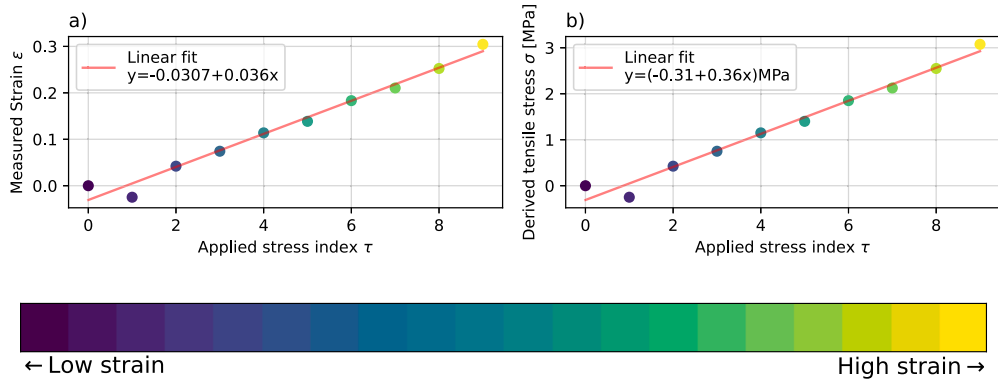


**Fig. 5.** Relationship between applied stress  $\tau$ , longitudinal stress  $\sigma$ , and strain  $\epsilon$ . The Young’s modulus of tape,  $E = \sigma/\epsilon = 10.1$  MPa was used to derive  $\sigma$ , while  $\epsilon$  was measured with our PS-OCT system and  $\tau$  was applied with our 3D printed stretcher. The red lines represent a linear fit between  $\epsilon$  and  $\tau$  (a) or  $\sigma$  and  $\tau$  (b), both with an  $R^2 = 0.996$ . On the bottom, the color code used to identify the different applied stress  $\tau$  levels is shown. Darker colors represent low-stress values, while higher ones are depicted by lighter colors.

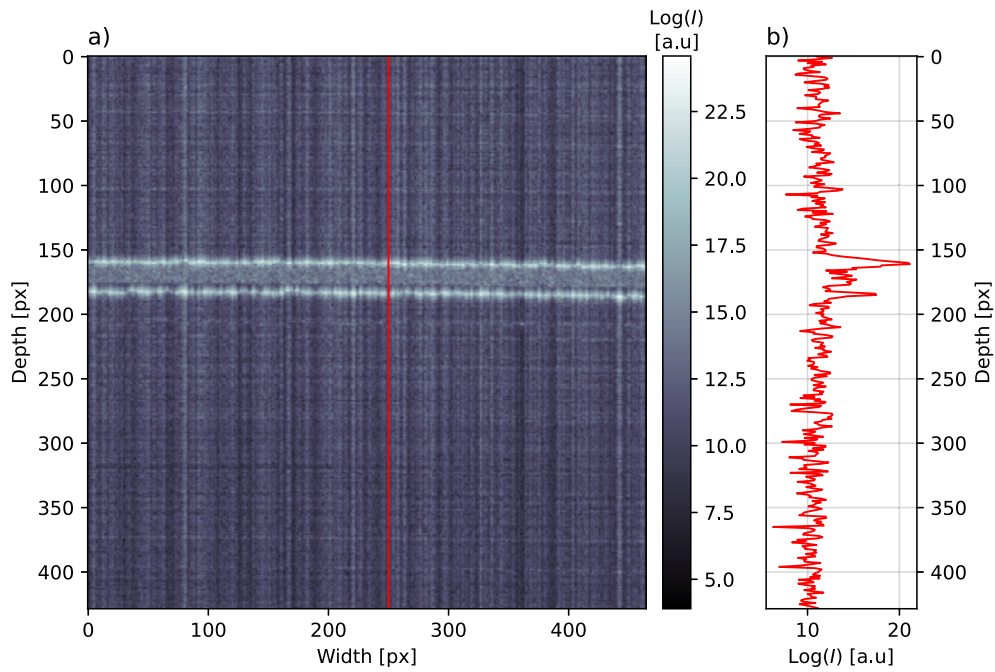


**Fig. 6.** Cross-section (B-scan) of the tape as viewed by the PS-OCT system (a) with a reference A-Scan marked in red (b). The first peak in the A-scan corresponds to the air-tape interface and the second one to the exit tape-air interface.

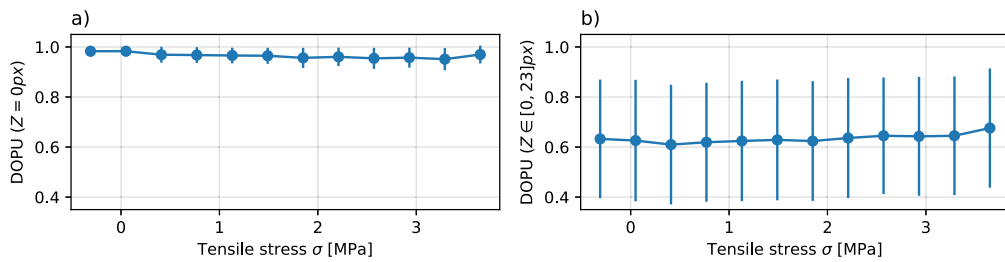


**Fig. 7.** Changes in  $DOPU$  as calculated with PS-OCT for the different strain conditions. The average is represented by the scatter points and the standard deviation by the error bars. On (a), only the values at the surface of the sample were considered ( $Z = 0$  px) and, on (b), the  $DOPU$  across all  $Z$  values inside the sample are represented ( $Z \in [0, 23]$  px). The standard deviation on (a) was, on average, of 0.033, while on (b) was 0.24. The vertical scale is the same for both graphs.

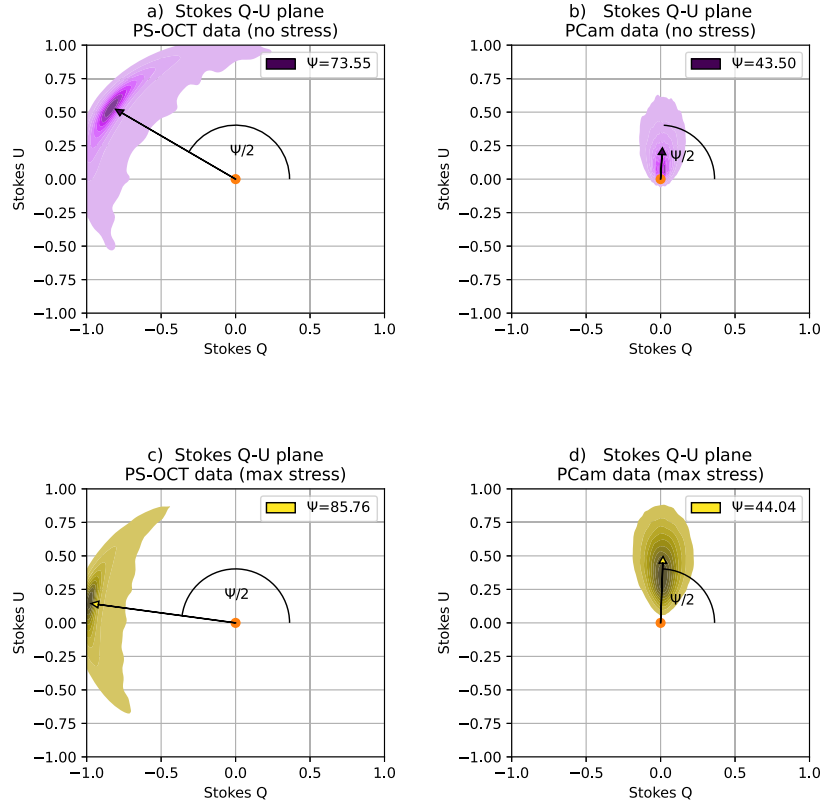


**Fig. 8.** PS-OCT (a,c) and PCam (b,d) density plots of the polarimetric measurement points of a strip of tape under no stress (a,b) and with maximum stress applied (c,d) prior to breaking.

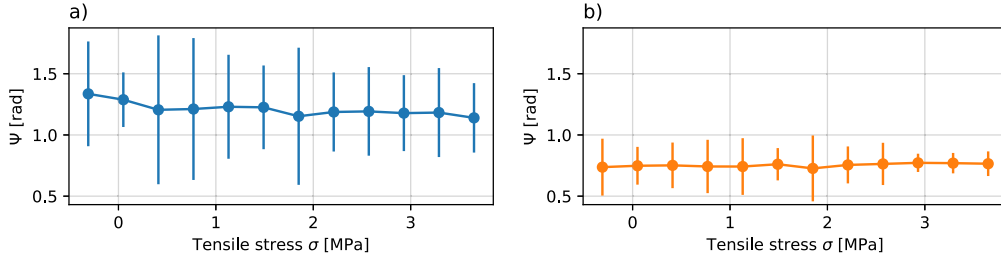


**Fig. 9.** Average (scatter points) and standard deviation (error bars) of  $\Psi$  for PS-OCT (a) and PCam (b) measurements. Greater variation of  $\Psi$  is shown in the PS-OCT images. The standard deviation on (a) was, on average, 0.40 rad, while on (b) was 0.17 rad. The vertical scale is the same for both graphs.

PS-OCT measurements, while the PCam captures a more symmetric distribution.

To further analyze how much the angle  $\Psi$  changes with stress, the average value of  $\Psi$  is calculated, as well as its standard deviation  $\sigma(\Psi)$ , for both systems (Fig. 9). The standard deviation can be interpreted as a measure of how spread the cloud of points is. We found that the standard deviation for the surface of the tape ( $Z = 0$  px) as measured by the PS-OCT system was, on average, 0.40 rad. For the PCam system, the standard deviation was 0.17 rad, which is 2.35 times smaller. Repeating this procedure by using all  $Z$  values inside the sample, the standard deviation for the PS-OCT device increased up to 0.71 rad, which is consistent with the loss of DOPU previously indicated.

We derived the remaining angles by equations (7), (8) and (9) and compared the results obtained by both systems. Initially, no correlation between the angles was found; the data points did not follow any kind of linear or non-linear relationship either between systems or with respect to the applied strain. Therefore, we proposed a different approach. Instead of comparing the angles at the individual  $\tau$  conditions, we analyzed the overall change in polarization up to a  $\tau$  value. Given

a variable  $\beta$  and a stress state  $\tau_n$ , the overall accumulated value of  $\beta$ ,  $\beta_{acc}$ , is defined as  $\beta_{acc} = \sum_{\tau=0}^{\tau_n} \beta(\tau)$  (Fig. 10).

Given that the relationship of the accumulated angles between the two systems is now apparently linear ( $\beta_{acc,PSOCT} \propto \beta_{acc,PCam}$ ), we fitted the data to a linear model ( $y = a + b \cdot x$ ) and obtained the values of the origin (a) slope (b) for each angle (Table 1). The coefficient of determination ( $R^2$ ) for all models was  $R^2 > 0.99$ , and the relative root mean squared error (RRMSE) was  $RRMSE < 0.5\%$  for the four angular relationships. The highest slope achieved was for  $\Psi_{acc}$  with  $b \approx 1.6$ , followed by  $\delta_{acc}$  and  $\alpha_{acc}$  with  $b \approx 0.35$  and, finally, by  $\chi_{acc}$  with  $b \approx 0.14$ . All models had an intercept value close to zero.

In Fig. 10 the stress index  $\tau$  is indicated as a color for each measurement. Since both PS-OCT and PCam measurements increase when  $\tau$  increases ( $\beta_{acc,PSOCT} \propto \tau$  and  $\beta_{acc,PCam} \propto \tau$ ), a linear model was used again to describe the relationship between the individual accumulated angles and the applied stress (Table 2). Again, the value of the coefficient of determination for all models was  $R^2 > 0.99$  and the RRMSE had values lower than 1% for all PS-OCT measurements and RRMSE lower than 0.5% for their PCam analogs.

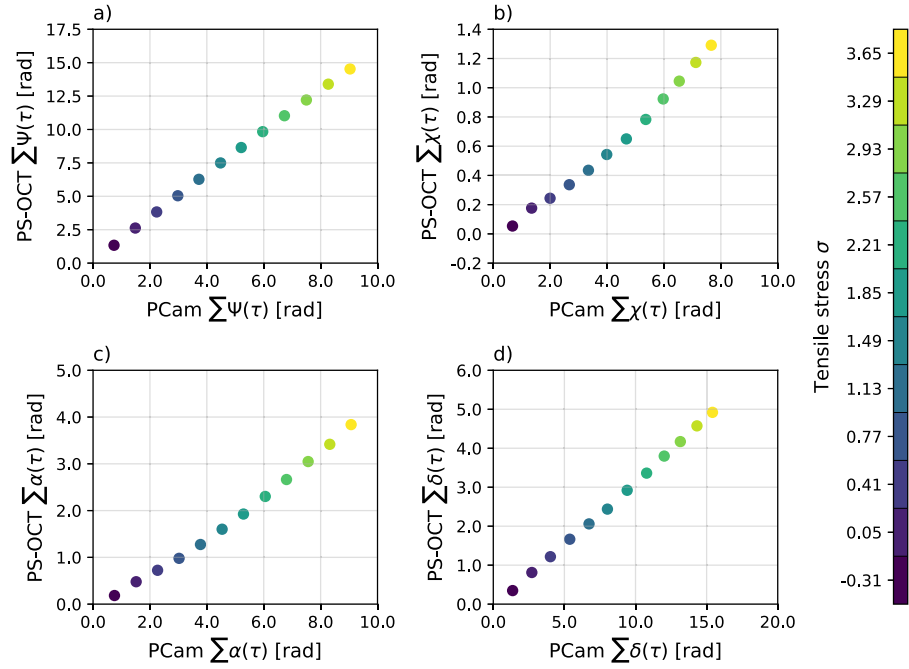


Fig. 10. Average values of the cumulative increment of  $\Psi$  (a),  $\chi$  (b),  $\alpha$  (c) and  $\delta$  (d), at different stress conditions, comparing PS-OCT and PCam measurements.

Table 1

Results of fitting the accumulated (*acc*) versions of the different angles to a linear model. The coefficient of determination  $R^2$  and relative root mean squared error (RRMSE) was calculated between the expected output and the actual output for each model.

$\Psi_{acc}(\tau) _{PSOCT} = a + b \cdot \Psi_{acc}(\tau) _{PCam}$	$\chi_{acc}(\tau) _{PSOCT} = a + b \cdot \chi_{acc}(\tau) _{PCam}$
$a = 0.203 \pm 0.085$ [rad]	$a = -0.0786 \pm 0.0091$ [rad]
$b = 1.609 \pm 0.015$	$b = 0.1388 \pm 0.18$
$R^2 = 0.999$	$R^2 = 0.992$
RRMSE = 0.42%	RRMSE = 0.43%

$\delta_{acc}(\tau) _{PSOCT} = a + b \cdot \delta_{acc}(\tau) _{PCam}$	$\alpha_{acc}(\tau) _{PSOCT} = a + b \cdot \alpha_{acc}(\tau) _{PCam}$
$a = -0.152 \pm 0.065$ [rad]	$a = -0.156 \pm 0.032$ [rad]
$b = 0.3403 \pm 0.0053$	$b = 0.3602 \pm 0.0076$
$R^2 = 0.994$	$R^2 = 0.998$
RRMSE = 0.36%	RRMSE = 0.16%

Table 2

Results of fitting the accumulated (*acc*) versions of the different angles to the stress index  $\tau$  through a linear model for the PS-OCT (top) and PCam (bottom) systems.

$\Psi_{acc}(\tau) _{PS-OCT} = a + b \cdot \tau$	$\chi_{acc}(\tau) _{PS-OCT} = a + b \cdot \tau$
$a = -0.43 \pm 0.11$ [rad]	$a = 0.078 \pm 0.012$ [rad]
$b = 1.005 \pm 0.015$	$b = 0.1174 \pm 0.0010$
$R^2 = 0.998$	$R^2 = 0.999$
RRMSE = 0.76%	RRMSE = 0.77%

$\delta_{acc}(\tau) _{PS-OCT} = a + b \cdot \tau$	$\alpha_{acc}(\tau) _{PS-OCT} = a + b \cdot \tau$
$a = 0.385 \pm 0.054$ [rad]	$a = 0.363 \pm 0.041$ [rad]
$b = 0.4964 \pm 0.0083$	$b = 0.2871 \pm 0.0063$
$R^2 = 0.997$	$R^2 = 0.997$
RRMSE = 0.33%	RRMSE = 0.65%

$\Psi_{acc}(\tau) _{PCam} = a + b \cdot \tau$	$\chi_{acc}(\tau) _{PCam} = a + b \cdot \tau$
$a = 0.72 \pm 0.13$ [rad]	$a = 0.745 \pm 0.015$ [rad]
$b = 0.753 \pm 0.021$	$b = 0.6428 \pm 0.0024$
$R^2 = 1.00$	$R^2 = 0.999$
RRMSE = 0.094%	RRMSE = 0.43%

$\delta_{acc}(\tau) _{PCam} = a + b \cdot \tau$	$\alpha_{acc}(\tau) _{PCam} = a + b \cdot \tau$
$a = 1.500 \pm 0.054$ [rad]	$a = 0.755 \pm 0.041$ [rad]
$b = 1.2927 \pm 0.0083$	$b = 0.7562 \pm 0.0063$
$R^2 = 0.999$	$R^2 = 1.00$
RRMSE = 0.43%	RRMSE = 0.016%

#### 4. Discussion

The polarization state of light reflected off adhesive tape was measured for different stress conditions with both PS-OCT and PCam setups. Initially, no apparent visual correlation between the two systems was found (Fig. 8). While PS-OCT measurements were close to the polarimetric sphere's edge with  $Q < 0$ , PCam measurements stayed as a cloud around  $Q = 0, U > 0$ . Generally speaking, the normalized ( $Q, U$ ) values have a more symmetrical and less dispersed distributions in the case of the PCam than the PS-OCT (Fig. 9). This may happen because, while the PS-OCT system uses circularly polarized light to excite every direction of the sample, the PCam is using linearly polarized light that might not be suffering the same polarimetric effects, giving rise to different projections over the  $Q - U$  plane.

The differences in the angles (particularly  $\Psi$ ) and their standard deviation between both systems are expected (Fig. 9), considering that these measurements are inherently different from each other. On the one hand, PS-OCT allows us to calculate the Stokes parameters at the surface of the tape ( $Z = 0$  px) or through all of its volume ( $Z \in [0, 23]$  px), while PCam measurements are integrated and, therefore, averaged over depth. Depth averaging could result in more homogeneous values of  $\Psi$ , which could explain the lower standard deviation in

the PCam results with respect to their PS-OCT counterparts. Additionally, different wavelengths are being used in each system: PS-OCT is operating at 1300 nm whereas PCam is acquiring at 435 nm. Considering the wavelength only, this means that backscattering and, therefore, signal power will be stronger for PCam than for PS-OCT. For the latter, the strongest signal will be at the surface, and decay in signal, as the laser penetrates the sample in PS-OCT, can deteriorate the value of the polarimetric properties. Furthermore, scotch tape presents a significant level of roughness that is much more apparent with the non-averaged PS-OCT signal than with PCam. Despite all these phenomena we have seen that it is possible to find a relationship between both modalities.

When comparing the angles between both systems for different stress conditions we found what appeared to be randomly distributed clouds of data that were transformed into a linear relationship by studying the cumulative change in the angles instead (Fig. 10). The initial random appearance of the data can be caused by the periodical nature of the angles. Two angles that have a  $\{\pm 2n\pi \mid n \in \mathbb{R}\}$  difference will provide the same values of  $(I, Q, U, V)$ . By using the sum of the values instead, we are unwrapping the angular signals so that we can remove the periodicity associated with them and compare them between systems accurately.

We assumed a linear relationship  $y = a + bx$  between the accumulated angles calculated with the PS-OCT and PCam data (Table 1). We found that  $\Psi_{acc}$  for the PS-OCT data increases faster than its PCam counterparts ( $b > 1$ ), while for the remaining angles, the opposite happens ( $b < 1$ ). The calculated coefficients of determination ( $R^2$ ) indicated a highly linear relationship between both systems ( $R^2 > 0.99$ ). The obtained root mean squared error (RRMSE) suggests that one could transform the results obtained by the PCam and the PS-OCT into each other with high accuracy (RRMSE < 0.5%).

When assuming a linear behavior not only between the angles of the two systems, but also with respect to the applied stress (Table 2), we found very similar values for the  $R^2$ , all greater than 0.99 and even 0.9995 for some angle-stress pairs. The RRMSE values indicate a low error on the calculations of the PS-OCT linear models, with RRMSE < 1%, and even less error in the case of the PCam models, with RRMSE < 0.5%.

After repeating the previously mentioned experiments by using all of the  $Z$  planes of PS-OCT inside the sample no significant change in behavior was apparent; the accumulative angles were still linearly correlated between systems with  $R^2 > 0.99$ . The data distributions for the angles were wider and their standard deviation was greater, which is expected when having more data points.

The linear models between the polarimetric angles and the applied stress index  $\tau$  are, in essence, stain-stress curve analogs. Because of that, these linear models are sample-dependent since the elongation and, therefore, the changes in polarimetric magnitudes, are determined by the Young's modulus of that specific sample. A sample that had little to no elastic behavior and only plastic deformation when under stress could present a completely different problem that might need a different curve to describe its angle-stress model.

Nevertheless, these kinds of experiments can be performed to analyze the elastic behavior of a sample as long as the stress applied is known, with the benefits of not having to use a bulky tensile stress machine and even being able to lower the price of the test device to that of a polarimetric camera, a polarized light source and a lens.

## 5. Summary

We conducted a series of experiments on adhesive tape and measured its polarimetric properties during the tests with two commercially available devices: a Polarization-Sensitive Optical Coherence Tomography setup and a polarimetric camera.

Since our systems do not share a light source, the Stokes parameters that we obtained are not initially comparable between them, so we evaluated instead the evolution of the polarimetric angles with stress. By studying the accumulative change in the angles via adding the individual angle increment for each applied strain, the relationship between the accumulated angles for the PS-OCT and PCam devices became highly linear. This means that any stress test that is performed in one of the systems can be easily translated to the other. That equivalence between systems could be a powerful tool in material science and fabrication since an in-depth micrometric analysis of a sample, performed with a PS-OCT system, can be up-scaled to an evaluation of identical samples, with the aid of a PCam, while keeping the relationship between the macroscopic and microscopic polarimetric properties. This equivalence between polarimetric properties could facilitate the

transition of laboratory experiments to manufacturing, the comparison of results between different research groups, establish repeatability and replicability protocols in applied research, and minimize setup costs in a variety of applications.

## CRedit authorship contribution statement

**Verónica Mieites:** Conceptualization, Data curation, Formal analysis, Investigation, Methodology, Software, Validation, Visualization, Writing – original draft, Writing – review & editing. **José A. Gutiérrez-Gutiérrez:** Software. **Arturo Pardo:** Methodology, Software, Writing – review & editing. **José M. López-Higuera:** Funding acquisition. **Olga M. Conde:** Conceptualization, Funding acquisition, Methodology, Project administration, Resources, Supervision, Writing – review & editing.

## Declaration of competing interest

The authors declare the following financial interests/personal relationships which may be considered as potential competing interests:

Veronica Mieites (PREVAL 21-07) reports financial support, administrative support, and travel were provided by Valdecilla Research Institute (IDIVAL). Olga M. Conde (DTS22-00127) reports financial support, administrative support, article publishing charges, equipment, drugs, or supplies, and travel were provided by Carlos III Health Institute. Olga M. Conde (EQC 2019-006589-P) reports financial support and equipment, drugs, or supplies were provided by Ministry of Science Technology and Innovations (Spanish State Research Agency). Jose M. Lopez-Higuera (PID2019-107270RB-C21\_AEI\_10.13039\_408\_501100011033) reports financial support and equipment, drugs, or supplies were provided by Ministry of Science Technology and Innovations (Spanish State Research Agency). Olga M. Conde (DTS22-00127, FEDER “A way to make Europe”) reports financial support and article publishing charges were provided by European Union.

## Data availability

Data will be made available on request.

## Acknowledgments and funding

Support for this work was provided by the projects PREVAL 21/07 (FUSIOMUSCLE) from IDIVAL, DTS22-00127 (hyPERfusioCAM) funded by Instituto de Salud Carlos III (ISCIII) and co-funded by the European Union; EQC 2019-006589-P, and PID2019-107270RB-C21/AEI/10.13039/501100011033) and FEDER “A way to make Europe”.

## Appendix A. Polarimetric magnitudes from the Stokes parameters

This section contains the derivation for the expressions of  $(\Psi, \chi, \alpha, \delta)$  that were used in the main manuscript to compare the polarimetric behavior of light obtained with the two used devices: PS-OCT and PCam. With the PS-OCT equipment we can measure  $(I, Q, U, V)$  and, with the PCam, only  $(I, Q, U)$ , which is why we are going to dedicate this section to finding every polarimetric variable possible with only the first three out of the four Stokes parameters.

We start with the two versions of the Stokes parameters [36,37] (equations (A.1)-(A.5)):

$$\left. \begin{aligned} S_0 &= I = \langle E_h^2 \rangle + \langle E_v^2 \rangle = I_h + I_v \\ S_1 &= Q = \langle E_h^2 \rangle - \langle E_v^2 \rangle = I_h - I_v \\ S_2 &= U = \langle E_{45}^2 \rangle - \langle E_{135}^2 \rangle = I_{45} - I_{135} \\ S_3 &= V = \langle E_l^2 \rangle - \langle E_r^2 \rangle = I_l - I_r \end{aligned} \right\} \text{Stoke's parameters} \quad (\text{A.1})$$

$$S_0 = I = a_1^2 + a_2^2 = a^2 + b^2 \quad (\text{A.2})$$

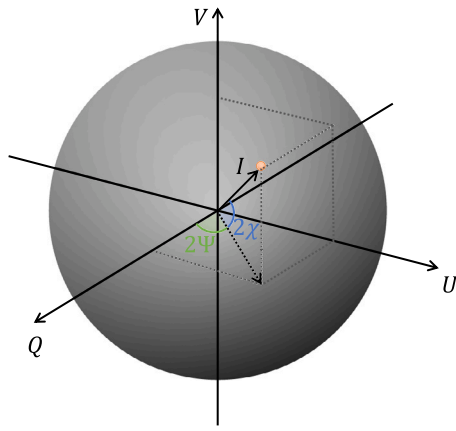


**Fig. A.11.** Poincaré's sphere representation for the Stokes parameters. Each of the  $Q$ ,  $U$  and  $V$  represent one of the spatial axis and  $I$  is the radius of the sphere. Each of the individual possible light states (orange point) represent one point on the surface of the sphere. If light is partially polarized, the corresponding states will be inside the sphere instead. Natural light sits at the origin of the coordinate system.

$$S_1 = Q = a_1^2 - a_2^2 = S_0 \cdot \cos(2\chi) \cdot \cos(2\Psi) \quad (\text{A.3})$$

$$S_2 = U = 2a_1 a_2 \cdot \cos(\delta) = S_0 \cdot \cos(2\chi) \cdot \sin(2\Psi) \quad (\text{A.4})$$

$$S_3 = V = 2a_1 a_2 \cdot \sin(\delta) = S_0 \cdot \sin(2\chi) \quad (\text{A.5})$$

Since we work with the  $I$ -normalized versions of  $(I, Q, U, V)$ ,  $(\bar{I}, \bar{Q}, \bar{U}, \bar{V})$ , these variables are defined in the following domains:

$$\left[ \bar{I} = \frac{I}{I_{max}} \in [0, 1] ; \bar{Q} = \frac{Q}{I} \in [-1, 1] ; \bar{U} = \frac{U}{I} \in [-1, 1] ; \bar{V} = \frac{V}{I} \in [-1, 1] \right]$$

It is worth noting that, by Eqs. (A.2), (A.3), (A.4) and (A.5), these variables can be defined in a sphere of radius 1 (or  $I_{max}$ , if we are not using the normalized versions) called Poincaré's sphere (Fig. A.11) [36,37], as per the relationship between them and the spherical coordinate system equations. Polarized light will be represented as a point on the surface of the sphere, ( $I^2 = Q^2 + U^2 + V^2$ ), while partially polarized light sits inside the sphere instead ( $I^2 > Q^2 + U^2 + V^2$ ). The concept of Poincaré's sphere will be useful to understand the domain of the polarization angles.

### A.1. Finding $\Psi$ and $\chi$

We derive  $\Psi$  from  $(Q, U)$  through equations (A.3) and (A.4) as:

$$\frac{(A.4)}{(A.3)} \rightarrow \frac{U}{Q} = \frac{\sin(2\Psi)}{\cos(2\Psi)} = \tan(2\Psi)$$

$$\Psi = \frac{1}{2} \tan^{-1} \left( \frac{U}{Q} \right) \in \left[ -\frac{\pi}{2}, +\frac{\pi}{2} \right] \quad (\text{A.6})$$

It should be noted that, when calculating  $\Psi$ , it is necessary to know and keep the signs of  $Q$  and  $U$  individually so the quadrant value of  $\tan^{-1}$  is accurate. Numerically, many programming languages provide a function called `atan2(·, ·)` with this very purpose.

By using  $(\Psi, I, Q)$  or  $(\Psi, I, U)$  (eqs. (A.3) or (A.4)) we can obtain  $\chi$  as:

$$\chi \stackrel{(A.3)}{=} \frac{1}{2} \cos^{-1} \left( \frac{1}{\cos(2\Psi)} \frac{Q}{I} \right) \stackrel{(A.4)}{=} \frac{1}{2} \cos^{-1} \left( \frac{1}{\sin(2\Psi)} \frac{U}{I} \right) \in \left[ 0, \frac{+\pi}{4} \right] \quad (\text{A.7})$$

Note that we cannot obtain the full range of variation of  $\chi$  just from  $Q$  and  $U$  alone. Since we are using only one plane of the full Poincaré space, points that have symmetry with respect to that plane, i.e., points

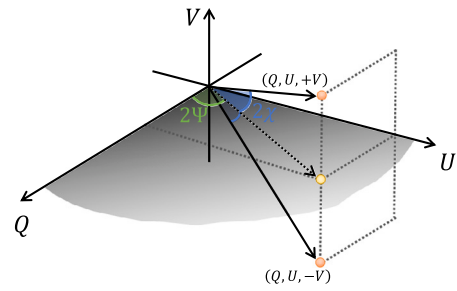


**Fig. A.12.** Two points on the Poincaré sphere (orange dots) will have the same projection over the plane  $(Q, U)$  (yellow dot) if the absolute value of their  $V$  coordinate is the same.

with the same  $V$  magnitude but with different sign, will have the same projection over the plane  $(Q, U)$  (Fig. A.12). To solve for the full  $\left[ -\frac{\pi}{4}, \frac{+\pi}{4} \right]$  range of  $\chi$ , we would need to use equation (A.5) instead of deriving it from  $Q$  and  $U$ .

### A.2. Finding $\delta$ and $\alpha$

We are going to use  $\Psi$  and  $\chi$  to find  $\delta$ . By definition,  $\chi$  and  $\alpha$  are derived from the polarization ellipse (Fig. 4) as

$$\tan(\chi) = \frac{b}{a} \quad (\text{A.8})$$

$$\tan(\alpha) = \frac{a_2}{a_1} \quad (\text{A.9})$$

where  $(a, b)$  are the major and minor axis of the ellipse and  $(2a_1, 2a_2)$  are the length of the sides of the rectangle that the ellipse is inscribed in.

By dividing both sides of  $U$  (A.4) by  $Q$  (A.3) we get the following:

$$\frac{(A.4)}{(A.3)} \rightarrow \frac{U}{Q} = \frac{2a_1 a_2 \cdot \cos(\delta)}{a_1^2 - a_2^2} = \frac{S_0 \cdot \cos(2\chi) \cdot \sin(2\Psi)}{S_0 \cdot \cos(2\chi) \cdot \cos(2\Psi)}$$

If we focus on the last equality and add  $a_2$  from (A.9)

$$\begin{aligned} (A.9) \rightarrow a_2 &= a_1 \cdot \tan(\alpha) \rightarrow \frac{2a_1^2 \cdot \tan(\alpha) \cdot \cos(\delta)}{a_1^2 (1 - \tan^2(\alpha))} \\ &= \frac{S_0 \cdot \cos(2\chi) \cdot \sin(2\Psi)}{S_0 \cdot \cos(2\chi) \cdot \cos(2\Psi)} \end{aligned}$$

which, by the tangent of the double-angle, is

$$\tan(2\alpha) \cdot \cos(\delta) = \tan(2\Psi) \quad (\text{A.10})$$

We still have two unknown variables in the previous equation,  $\alpha$  and  $\delta$ , so we need another equation to find both. To do so, we use  $V$  (A.5) and  $I$  (A.2) as follows:

$$\frac{(A.5)}{(A.2)} \rightarrow \frac{V}{I} = \frac{2a_1 a_2 \cdot \sin(\delta)}{S_0} = \frac{2a_1 a_2 \cdot \sin(\delta)}{a_1^2 + a_2^2} = \frac{S_0 \cdot \sin(2\chi)}{S_0}$$

and, again from (A.9)

$$(A.9) \rightarrow a_2 = a_1 \cdot \tan(\alpha) \rightarrow \frac{2a_1^2 \tan(\alpha) \cdot \sin(\delta)}{a_1^2 (1 + \tan^2(\alpha))} = \frac{S_0 \cdot \sin(2\chi)}{S_0}$$

Finally, by using the sine of the double-angle, we get our second equation

$$\tan(2\alpha) \cdot \sin(\delta) = \sin(2\chi) \quad (\text{A.11})$$

Next, we do a variable change to simplify the writing:

$$\begin{cases} n = \tan(2\Psi) \\ m = \sin(2\chi) \end{cases}$$

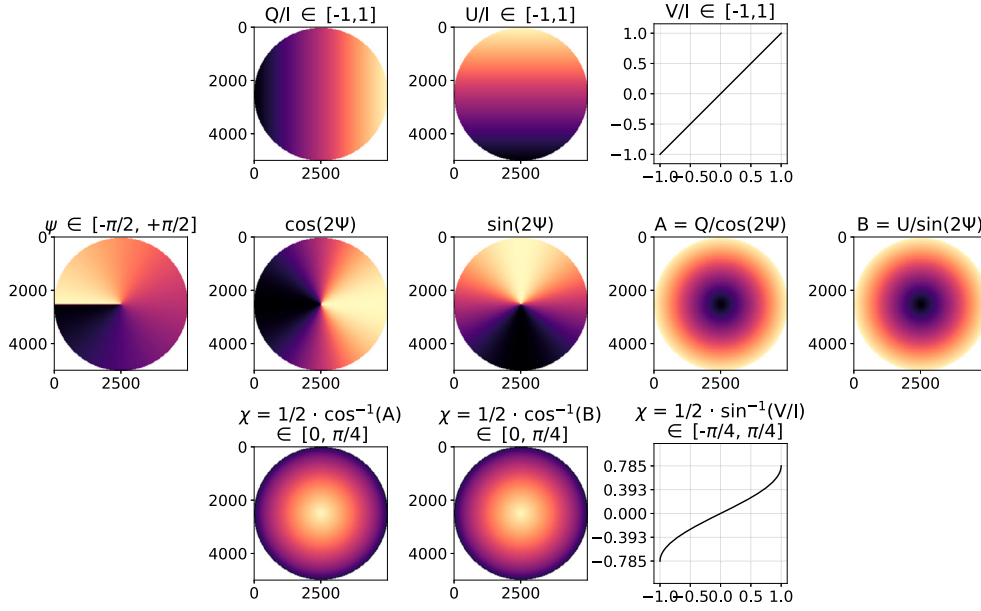


Fig. A.13.  $\Psi$  and  $\chi$  calculation from  $(Q, U, V)$  through equations (A.6), (A.7) and (A.5). Darker colors represent lower values, while lighter colors represent higher values.

so that the equation system to solve becomes:

$$\begin{cases} \tan(2\Psi) = \tan(2\alpha) \cdot \cos(\delta) \\ \sin(2\chi) = \sin(2\alpha) \cdot \sin(\delta) \end{cases} \rightarrow \begin{cases} n = \tan(2\alpha) \cdot \cos(\delta) \\ m = \sin(2\alpha) \cdot \sin(\delta) \end{cases} \quad (\text{A.12})$$

We divide  $m$  by  $n$

$$\frac{m}{n} = \frac{\sin(2\alpha) \cdot \sin(\delta)}{\tan(2\alpha) \cdot \cos(\delta)} = \cos(2\alpha) \cdot \tan(\delta) \rightarrow \cos(2\alpha) = \frac{m}{n} \frac{1}{\tan(\delta)}$$

and find  $\sin(2\alpha)$  from  $m$  (A.12)

$$\sin(2\alpha) = m \frac{1}{\sin(\delta)}$$

so that we can apply  $\sin^2(2\alpha) + \cos^2(2\alpha) = 1$ :

$$\begin{aligned} \sin^2(2\alpha) + \cos^2(2\alpha) &= 1 \\ \left(\frac{m}{\sin(\delta)}\right)^2 + \left(\frac{m/n}{\tan(\delta)}\right)^2 &= 1 \\ \left(\frac{m}{\sin(\delta)}\right)^2 + \left(\frac{m \cos(\delta)}{n \sin(\delta)}\right)^2 &= 1 \\ \left(\frac{m}{\sin(\delta)}\right)^2 + \left(\frac{m}{\sin(\delta)}\right)^2 \cdot \frac{\cos^2(\delta)}{n^2} &= 1 \\ \left(\frac{m}{\sin(\delta)}\right)^2 \cdot \left[1 + \frac{1}{n^2} \cos^2(\delta)\right] &= 1 \\ 1 + \frac{1}{n^2} \cos^2(\delta) &= \frac{1}{m^2} \sin^2(\delta) \\ 1 + \frac{1}{n^2} \cos^2(\delta) - \frac{1}{m^2} \sin^2(\delta) &= 0 \\ n^2 m^2 + m^2 \cdot \cos^2(\delta) - n^2 \cdot \sin^2(\delta) &= 0 \end{aligned}$$

From here, we switch to Euler's notation of  $\cos(x) = \frac{e^{ix} + e^{-ix}}{2}$  and  $\sin(x) = \frac{e^{ix} - e^{-ix}}{2i}$ , therefore the previous derivations continue out as follows:

$$\begin{aligned} n^2 m^2 + m^2 \left(\frac{e^{i\delta} + e^{-i\delta}}{2}\right)^2 - n^2 \left(\frac{e^{i\delta} - e^{-i\delta}}{2i}\right)^2 &= 0 \\ n^2 m^2 + \frac{m^2}{4} (e^{2i\delta} + e^{-2i\delta} + 2e^0) - \frac{n^2}{4} (e^{2i\delta} + e^{-2i\delta} - 2e^0) &= 0 \end{aligned}$$

$$n^2 m^2 + \frac{m^2}{2} + \frac{m^2}{4} (e^{2i\delta} + e^{-2i\delta}) - \frac{n^2}{2} + \frac{n^2}{4} (e^{2i\delta} + e^{-2i\delta}) = 0$$

$$n^2 m^2 + \frac{m^2}{2} - \frac{n^2}{2} + \left(\frac{m^2 + n^2}{4}\right) \cdot (e^{2i\delta} + e^{-2i\delta}) = 0$$

$$2n^2 m^2 + (m^2 - n^2) + (m^2 + n^2) \cdot \frac{1}{2} (e^{2i\delta} + e^{-2i\delta}) = 0$$

which, going back to regular  $\cos(x)$  notation, is

$$2n^2 m^2 + (m^2 - n^2) + (m^2 + n^2) \cos(2\delta) = 0$$

$$\cos(2\delta) = \frac{n^2 - m^2 - 2n^2 m^2}{m^2 + n^2}$$

Finally, we have our equation for  $\delta$

$$\delta = \frac{1}{2} \cos^{-1} \left( \frac{n^2 - m^2 - 2n^2 m^2}{m^2 + n^2} \right) \in \left[ 0, \frac{+\pi}{2} \right] \quad (\text{A.13})$$

that we can substitute with  $\Psi$  or  $\chi$  in either of the two (A.12) equations to find  $\alpha$  as

$$\alpha = \frac{1}{2} \sin^{-1} \left( \frac{\sin(2\chi)}{\sin(\delta)} \right) = \frac{1}{2} \tan^{-1} \left( \frac{\tan(2\chi)}{\cos(\delta)} \right) \in \left[ \frac{+\pi}{4}, \frac{+\pi}{2} \right] \quad (\text{A.14})$$

Again, as happened with  $\chi$ , we can only find a fraction of the full possible values of  $\alpha$  and  $\delta$  by only using  $Q$  and  $U$ , since we are not using the full polarimetric information.

### A.3. Ellipse axial length and rectangle sides length

Since we have every angle and three of the four Stokes parameters, we can find the length of the ellipse's axis ( $a, b$ ) and the rectangle's sides ( $a_1, a_2$ ). By taking into account the value of  $I$  (A.2), we can find ( $a, b$ ) from the definition of  $\chi$  (A.8):

$$(A.8) \rightarrow a \cdot \tan(\chi) = b$$

$$a^2 \cdot \tan^2(\chi) \stackrel{(A.2)}{=} I^2 - a^2$$

$$a^2 = \frac{I}{1 + \tan^2(\chi)} ; b^2 = \frac{I \cdot \tan^2(\chi)}{1 + \tan^2(\chi)} \quad (\text{A.15})$$

and, analogously, for ( $a_1, a_2$ ) from the definition of  $\alpha$  (A.9):

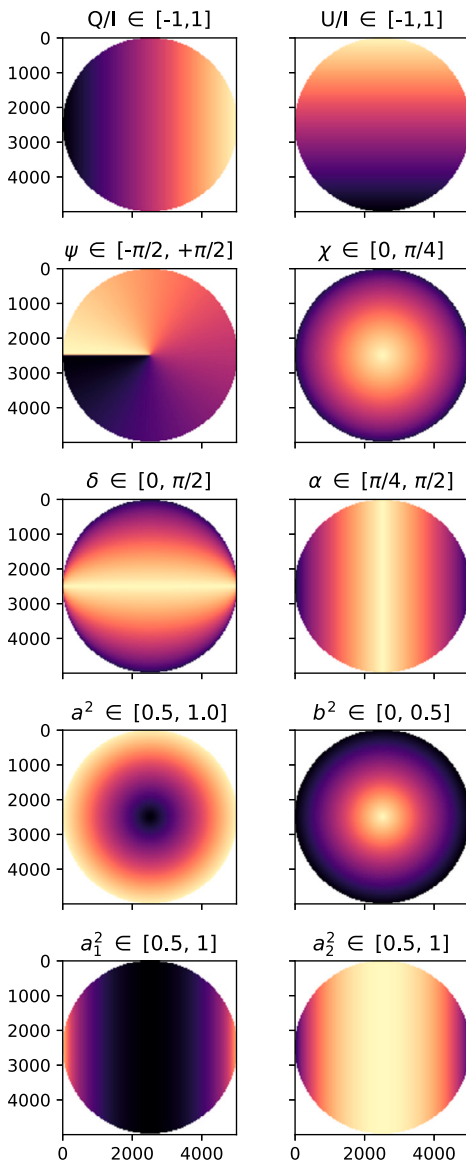


**Fig. A.14.** Polarimetric parameters calculation using  $Q$  and  $U$  through equations (A.6), (A.7), (A.14), (A.13), (A.15) and (A.16). Darker colors represent lower values, while lighter colors represent higher values.

$$(A.9) \longrightarrow a_1 \cdot \tan(\alpha) = a_2$$

$$a_1^2 \cdot \tan^2(\alpha) \stackrel{(A.2)}{=} I^2 - a_1^2$$

$$a_1^2 = \frac{I}{1 + \tan^2(\alpha)} ; a_2^2 = \frac{I \cdot \tan^2(\alpha)}{1 + \tan^2(\alpha)} \quad (A.16)$$

#### A.4. Examples

**Using  $Q$ ,  $U$  and  $V$**  We calculated every polarimetric parameter based on the normalized versions of  $Q$ ,  $U$  and  $V$ . First, we graphed  $\bar{Q}$ ,  $\bar{U}$ ,  $\bar{V}$ ,  $\Psi$  as obtained through equation (A.6), and  $\chi$  calculated through equations (A.7) and (A.5), as well as some intermediate steps. Results are shown in Fig. A.13. For  $Q$  and  $U$  we applied the condition  $Q^2 + U^2 \leq I^2$ , while we used the full possible values of  $V$  to calculate  $\chi$ . In Fig. A.13 is shown that we can find the full range of  $\chi$  only by using  $V$ , while by using  $Q$  and  $U$  we are only able to see its projection in the  $(Q, U)$  plane, as previously stated.

**Using  $Q$  and  $U$**  We simulated again  $\Psi$  and  $\chi$ , but also  $\delta$ ,  $\alpha$ ,  $(a_1, a_2)$  and  $(a, b)$ , but this time we used only the normalized versions of  $Q$  and

$U$ , as if they were measurements taken with the polarimetric camera. Again, we only calculated the parameters where  $Q^2 + U^2 \leq I^2$ . Results are shown in the following figure.

In Fig. A.14 we see again the same behavior for  $\Psi$  and  $\chi$  as shown in Fig. A.13. On the other hand, the values and obtained for  $(a, b)$  and  $(a_1, a_2)$  are consistent with the condition established in equation (A.2).

Since for  $\delta$  we obtain values between  $[0, \pi/2]$  we would be able to identify horizontal polarization ( $\delta = 0$ ), circular polarization ( $\delta = \pi/2$ ) and, generally speaking, left-handed polarized elliptical light ( $\delta \in [0, \pi]$ ). Nevertheless, since we are not using  $V$ , talking about left- or right-handed polarization would not be accurate given that both polarization states can have the same values of  $Q, U$ . Therefore, we compared PCam and PS-OCT measurements taking into account that we are using only the projection of the actual polarization states.

#### References

- [1] Podoleanu AG. Optical coherence tomography. *J Microsc* 2012;247(3):209–19. <https://doi.org/10.1111/j.1365-2818.2012.03619.x>. <https://onlinelibrary.wiley.com/doi/pdf/10.1111/j.1365-2818.2012.03619.x>.
- [2] Adhi M, Duker JS. Optical coherence tomography—current and future applications. *Curr Opin Ophthalmol* 2013;24(3):213–21.
- [3] Everett M, Magazzeni S, Schmoll T, Kempe M. Optical coherence tomography: from technology to applications in ophthalmology. *Transl Biophotonics* 2021;3(1):e202000012. <https://doi.org/10.1002/tbio.202000012>.
- [4] Thomas D, Duguid G. Optical coherence tomography—a review of the principles and contemporary uses in retinal investigation. *Eye* 2004;18(6):561–70. <https://doi.org/10.1038/sj.eye.6700729>.
- [5] Sampson DM, Dubis AM, Chen FK, Zawadzki RJ, Sampson DD. Towards standardizing retinal optical coherence tomography angiography: a review. *Light: Sci Appl* 2022;11(1):63. <https://doi.org/10.1038/s41377-022-00740-9>.
- [6] Suliali NJ, Baricholo P, Neethling PH, Rohwer EG. Non-destructive surface profilometry by first reflection localization using spectral domain optical coherence tomography. In: *Imaging and applied optics 2017* (3D, AIO, COSI, IS, MATH, pCAOP). Optica Publishing Group; 2017. p. JTU5A.29.
- [7] Cerrotta S, Morel E, Torga J. Scanning optical coherence tomography applied to the characterization of surfaces and coatings. *Proc Mater Sci* 2015;9:142–9. <https://doi.org/10.1016/j.mspro.2015.04.018>.
- [8] Kunicki-Goldfinger J, Targowski P, Góra M, Karaszkievicz P, Dzierzanowski P. Characterization of glass surface morphology by optical coherence tomography. *Stud Conserv* 2009;54(2):117–28.
- [9] Lee S, Hong S, Na J, Kim H, Jeong Y. Glass substrate inspection using swept-source optical coherence tomography. In: *Optical sensors and sensing congress (ES, FTS, HISE, sensors)*. Optica Publishing Group; 2019. p. JTh2A.24.
- [10] Sokolov M, Franciosa P, Sun T, Ceglarek D, Dimatteo V, Ascari A, et al. Applying optical coherence tomography for weld depth monitoring in remote laser welding of automotive battery tab connectors. *J Laser Appl* 2021;33(1):012028. <https://doi.org/10.2351/7.0000336>.
- [11] Jiang Z, Jiang Z, Ding H. Optical coherence tomography for laser welding applications. *Optik* 2022;257:168784. <https://doi.org/10.1016/j.ijleo.2022.168784>.
- [12] Bashkansky M, Reintjes JF. Subsurface detection and characterization of Hertzian cracks in advanced ceramic materials using optical coherence tomography. In: *Meyendorf N, Baaklini GY, Michel B, editors. Nondestructive evaluation and reliability of micro- and nanomaterial systems*. Proc SPIE, vol. 4703. International Society for Optics and Photonics; 2002. p. 46–52.
- [13] Matheus TCU, Kauffman CMF, Braz AKS, Mota CCBO, Gomes ASL. Fracture process characterization of fiber-reinforced dental composites evaluated by optical coherence tomography, sem and optical microscopy. *Braz Dent J* 2010;21:420–7. <https://doi.org/10.1590/S0103-64402010000500008>.
- [14] Kim K, Kim P, Lee J, Kim S, Park S, Choi SH, et al. Non-destructive identification of weld-boundary and porosity formation during laser transmission welding by using optical coherence tomography. *IEEE Access* 2018;6:76768–75. <https://doi.org/10.1109/ACCESS.2018.2882527>.
- [15] Ishibashi K, Ozawa N, Tagami J, Sumi Y. Swept-source optical coherence tomography as a new tool to evaluate defects of resin-based composite restorations. *J Dent* 2011;39(8):543–8. <https://doi.org/10.1016/j.jdent.2011.05.005>.
- [16] de Boer JF, Hitzberger CK, Yasuno Y. Polarization sensitive optical coherence tomography - a review [invited]. *Biomed Opt Express* 2017;8(3):1838–73.
- [17] Huang D, Swanson EA, Lin CP, Schuman JS, Stinson WG, Chang W, et al. Optical coherence tomography. *Science* 1991;254(5035):1178–81. <https://doi.org/10.1126/science.1957169>.
- [18] Wiesauer K, Dufau AS, Götzinger E, Pircher M, Hitzberger C, Stifter D. Non-destructive quantification of internal stress in polymer materials by polarisation sensitive optical coherence tomography. *Acta Mater* 2005;53(9):2785–91. <https://doi.org/10.1016/j.actamat.2005.02.034>.
- [19] Wiesauer K, Pircher M, Götzinger E, Hitzberger CK, Oster R, Stifter D. Investigation of glass-fibre reinforced polymers by polarisation-sensitive, ultra-high resolution optical coherence tomography: internal structures, defects and stress. *Compos*

- Sci Technol 2007;67(15):3051–8. <https://doi.org/10.1016/j.compscitech.2007.04.018>.
- [20] Stifter D, Burgholzer P, Höglinger O, Götzinger E, Hitzberger CK. Polarisation-sensitive optical coherence tomography for material characterisation and strain-field mapping. *Appl Phys A* 2003;76(6):947–51. <https://doi.org/10.1007/s00339-002-2065-5>.
- [21] Eom JB, Ahn JS, Eom J, Park A. Wide field of view optical coherence tomography for structural and functional diagnoses in dentistry. *J Biomed Opt* 2018;23(7):076008. <https://doi.org/10.1117/1.JBO.23.7.076008>.
- [22] Wolff LB, Andreou AG. Polarization camera sensors. *Image Vis Comput* 1995;13(6):497–510. [https://doi.org/10.1016/0262-8856\(95\)94383-B](https://doi.org/10.1016/0262-8856(95)94383-B).
- [23] Yamazaki T, Maruyama Y, Uesaka Y, Nakamura M, Matoba Y, Terada T, et al. Four-directional pixel-wise polarization cmos image sensor using air-gap wire grid on 2.5-um back-illuminated pixels. In: 2016 IEEE international electron devices meeting (IEDM); 2016. p. 8.7.1–4.
- [24] Hosoya N, Katsumata T, Kajiwara I, Onuma T, Kanda A. Measurements of s0 mode lamb waves using a high-speed polarization camera to detect damage in transparent materials during non-contact excitation based on a laser-induced plasma shock wave. *Opt Lasers Eng* 2022;148:106770. <https://doi.org/10.1016/j.optlaseng.2021.106770>.
- [25] Chen Y, Li Y, Wang Y, Mi Z, Wang Y, Fu X. Robust polarization-based underwater image enhancement method using anchor brightness adaptation. *Opt Lasers Eng* 2023;169:107737. <https://doi.org/10.1016/j.optlaseng.2023.107737>.
- [26] Deng J, Zhu J, Li H, Zhang X, Guo F, Hou X. Real-time underwater polarization imaging without relying on background. *Opt Lasers Eng* 2023;169:107721. <https://doi.org/10.1016/j.optlaseng.2023.107721>.
- [27] Han P, Liu F, Wei Y, Shao X. Optical correlation assists to enhance underwater polarization imaging performance. *Opt Lasers Eng* 2020;134:106256. <https://doi.org/10.1016/j.optlaseng.2020.106256>.
- [28] Lane C, Rode D, Rösger T. Optical characterization method for birefringent fluids using a polarization camera. *Opt Lasers Eng* 2021;146:106724. <https://doi.org/10.1016/j.optlaseng.2021.106724>.
- [29] Liang J, Tian X, Tu X, Spires O, Brock N, Wang D, et al. Color full Stokes polarization fringe projection 3d imaging. *Opt Lasers Eng* 2020;130:106088. <https://doi.org/10.1016/j.optlaseng.2020.106088>.
- [30] Luo Y, Zhang J, Tian D. Sparse representation-based demosaicking method for joint chromatic and polarimetric imagery. *Opt Lasers Eng* 2023;164:107526. <https://doi.org/10.1016/j.optlaseng.2023.107526>.
- [31] Xu Z, Zhang S, Han Y, Dong X, Su Z, Zhang D. Full-field phase shifting and stress quantification using a polarization camera. *Measurement* 2022;201:111727. <https://doi.org/10.1016/j.measurement.2022.111727>. <https://www.sciencedirect.com/science/article/pii/S0263224122009320>.
- [32] Tyo JS, Goldstein DL, Chenault DB, Shaw JA. Review of passive imaging polarimetry for remote sensing applications. *Appl Opt* 2006;45(22):5453–69. <https://doi.org/10.1364/AO.45.005453>.
- [33] Liberatore A, Fineschi S, Capobianco G, Massone G, Zangrilli L, Nicolini G, et al. PolarCam micropolarizer cameras characterization and usage. In: Cugny B, Sodnik Z, Karafolas N, editors. International conference on space optics — ICSSO 2020. *Proc SPIE*, vol. 11852. International Society for Optics and Photonics; 2021. p. 118520W.
- [34] Chang J, He H, He C, Ma H. DoFP polarimeter based polarization microscope for biomedical applications. In: Tuchin VV, Larin KV, Leahy MJ, Wang RK, editors. Dynamics and fluctuations in biomedical photonics XIII. *Proc SPIE*, vol. 9707. International Society for Optics and Photonics; 2016. p. 97070W.
- [35] Yin Z, Zou H. A fast and simple bonding method for low cost microfluidic chip fabrication. *J Electr Eng* 2018;69(1):72–8. <https://doi.org/10.1515/jee-2018-0010>.
- [36] Born M, Wolf E, Bhatia A. Principles of optics: electromagnetic theory of propagation, interference and diffraction of light. Cambridge University Press; 2000.
- [37] Hecht E. Optics. Pearson education. Addison-Wesley; 2002.